Laboratory simulation of space weathering on silicate surfaces in water environment

Mara Murri, Giancarlo Capitani, Mauro Fasoli, Angelo Monguzzi, Alberto Calloni,*

*Gianlorenzo Bussetti, Nadia Malaspina, Marcello Campione**

KEYWORDS: nanosecond pulsed laser ablation, laser peening, silicate surfaces, silicate nanoparticles, volatile-rich body, optical spectroscopy, X-ray photoelectron spectroscopy, transmission electron microscopy

ABSTRACT

Silicate nanoparticles occur in various astrophysical environments where they experience substantial processing due to events such as grain-grain collisions and irradiation. However, the structure and chemical evolution together with the origin of these grains are still poorly understood and intensively debated. For this purpose, we performed liquid-phase nanosecond pulsed laser

ablation on olivine single crystals to (i) simulate space weathering in a water environment (e.g., hydrous or volatile-rich bodies) and (ii) study the chemical and structural evolution of both the target surface and the ablated material. In particular, optical spectroscopy analyses have been performed on the ablated material and correlated with high-resolution transmission electron microscopy and diffraction; whereas, compositional variations of the ablated target surface were determined by X-ray photoelectron spectroscopy. Our results show that the target material is enriched in Fe and depleted in Mg after the ablation process, with the water environment triggering the oxidation of Fe^{2+} into Fe^{3+} in a region confined at the solid-liquid interface and thus promoting the formation of magnetite on the sample surface. On the other hand, in the ablated material we find olivine crystalline fragments with shock features together with Mg-rich crystalline nanoparticles. Notably, no metallic iron nanoparticles have been detected in the ablated material. Our simulation of space weathering in water environment revealed structural and chemical changes which are expected to give rise to distinctive features in the reflectance spectra when compared to those from airless bodies of the inner Solar System.

GRAPHICAL ABSTRACT

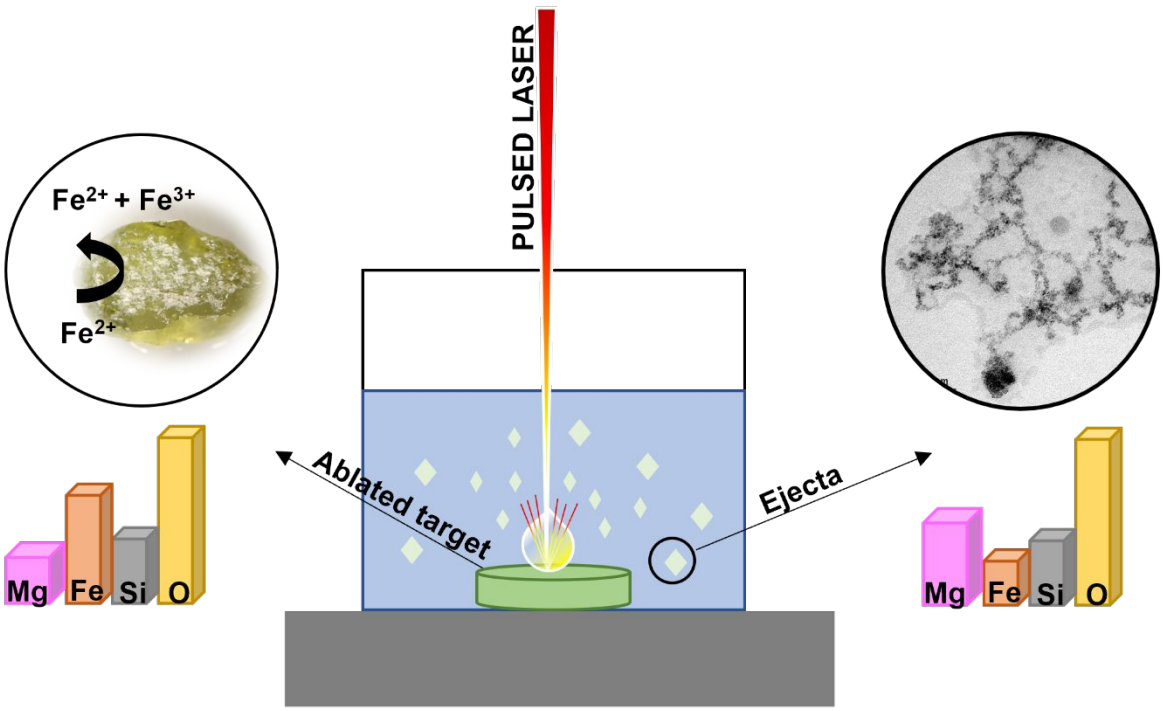

INTRODUCTION

Dust grains occur in various astrophysical environments (i.e., from comets to the farthest known galaxies) being the major responsible of a large variety of processes in the interstellar medium [1,2]. Indeed, thanks to their high surface-to-volume ratio, they act as catalytic substrates for the formation of common and complex molecules and their structure (i.e., crystalline or amorphous), size and shape, play a fundamental role in the surface reactivity [3,4]. In particular,

according to ref [5], interstellar grains are divided into three main size domains in accordance with the ranges 1000-100 nm, 100-5 nm, and 5-0.3 nm. In the context of materials science and engineering, particles with a size included in the last two ranges are referred to as nanoparticles, a term used to indicate a substantial distinction of the material properties with respect to those of the bulk phase. Furthermore, particles with a size included in the last range are also usually referred to as Very Small Grains (VSGs), in accordance with the terminology employed in planetary sciences. VSGs are those with the highest relative abundance among interstellar grains.

Among dust grains, the silicates are the most common species [6,7]. The existence of interstellar silicate grains was first proposed by Kamijo in 1963 [8] and a few years later they were detected in several cosmos regions. The broad infrared (IR) feature detected around 10 μm corresponding to the Si-O stretching mode suggests that most silicate grains in the interstellar medium are amorphous. However, the new advanced spectrometers coupled with the development of the Infrared Space Observatory (ISO) revealed the presence of crystalline silicates around comets, dust disks and in interplanetary dust particles (see ref [9] and references therein). These grains experience a strong structural modification during their lifetime in the diffuse interstellar medium due to events such as grain-grain collisions and irradiation. Grain amorphization is one of

the major effects, transforming crystalline silicate grains concentrated in star envelopes into amorphous material populating the interstellar medium [10]. However, after the amorphization process, residual crystalline features could be still retained giving rise to a population of crystalline silicate nanoparticles occurring in the interstellar regions [11]. Moreover, it cannot be ruled out also the possibility that the crystalline size domains of the nanoparticles are below the detection limit of the available spectroscopic techniques.

The main building blocks of the interstellar silicates are O, Si, Fe, Mg, Al and Ca; all elements that are among the principal constituents of the Earth's surface [12], thus leading to the name "astronomical silicates". Moreover, the comparison of acquired IR spectra with laboratory ones provided the necessary information to confirm that astronomical silicates have mainly olivine and pyroxene composition [7,11,13,14].

The persistent space weathering processes these astronomical silicate grains experience in the outer space (e.g., from irradiation, ion bombardment to impact shock events) might cause also irreversible chemical changes [15]. These changes are still poorly understood and characterized given the difficulties in reproducing the pertinent atmospheres and environments and the limited instrumental resolution of remote sensing data. However, understanding the effects of these

processes is of fundamental importance (i) for the correct interpretation of remote sensing data and (ii) to increase the knowledge on nanoparticles vs bulk material properties [7].

For this purpose, space weathering processes have always been the subject of experimental and theoretical studies [1,15-19] aimed at simulating the physical and optical properties of interstellar dust grains and the surface alteration of planetary bodies [4,10,11,20-23]. In particular, irradiation with high energy ions (e.g., H^+, He^+), nano- and femtosecond pulsed laser ablation have been carried out in vacuum on selected silicate samples (e.g., powder, single crystals, pellets) to reproduce the effects of solar wind radiation and shock events on airless bodies [10,16,17,22,24-26].

Furthermore, hydrous or volatile-rich bodies with distinct amounts of H and OH such as Vesta, Ceres, are also subjected to space weathering processes [15,27-30]. However, these bodies, despite being airless, do not exhibit a measurable content of metallic iron particles on their surface. This evidence has been attributed to a lesser flux of solar wind and meteoroid bombardment with respect to Moon or Mercury [15,29]. Moreover, dust/ice agglomerates are known to populate dense molecular clouds, comets and planet-forming disks (e.g., evidence from samples returned by the Stardust mission [31] and data obtained from the Rosetta mission [32]). For examples, the recent results

by Potapov et al. [33,34] showed that silicate grains can entrap water ice molecules at 8 K giving rise to stable silicate agglomerates mixed with ice up to 200 K when the water molecules start to desorb.

Even though space weathering processes are receiving more and more attention, the role of volatile species in space weathering together with the structural-chemical evolution and the origin of these cosmic silicates are still poorly understood and intensively debated [7,30,35].

Therefore, the aim of this study is the experimental simulation of space weathering processes by liquid-phase nanosecond pulsed laser ablation (LP-PLA) on olivine single crystals to shed light on the structure and chemical evolution of both the impacted silicate target and the ejected/ablated material in a water environment.

Laser ablation is usually performed in vacuum or inert atmosphere, but an alternative configuration was proposed by Patil et al. [36] where the target is immersed in a liquid medium, and the high intensity laser beam is focused through the liquid onto the surface of the target. This procedure is also widely used to synthesize nanoparticles in a clean environment with respect to chemical synthesis methods, thus providing several advantages in both laboratory and industrial applications [37,38]. In LP-PLA, the interaction of the high intensity laser pulse with the target surface produces an ablation plume of ejected material, in which the surface of the solid target and a small

amount of the surrounding liquid are vaporized to form bubbles until they collapse with substantial increment of the cooling rates with respect to air or vacuum, giving rise to products in the form of nanoparticles suspended within the liquid medium. This allows either for their simple retrieval by filtration and evaporation of the liquid, or for their further laser processing [39]. The tamping effect of the liquid layer allows for the control of the ablation rate while incrementing local pressure, with some advantages in terms of control of nanoparticle size distribution, shape and structure [40,41]. On the other side, the remnant target represents a useful product of the extreme conditions induced during the plasma recoil effects (laser peening).

This work has been carried out by means of a multiple technique characterization in order to investigate the chemical-physical properties of both the shocked target surface and the ablated nanoparticles. X-ray Photoelectron Spectroscopy (XPS) analyses have been carried out to analyze the surface chemical composition and speciation of the target material before and after laser treatment. High-resolution transmission electron microscopy (HR-TEM) coupled with optical spectroscopy and dynamic light scattering measurements have been performed on colloidal solutions of the ablated nanoproducts. Analyses of their electrostatic properties and acid/base reactivity have been also carried out for a deeper chemical characterization. Our results show that

a substantial chemical processing might be expected in both interstellar grains and silicate surfaces during space weathering processes in water environments, having distinctive features with respect to space weathering occurring in vacuum environment. This study provides also additional tools for (i) the identification of grains of different origin by means of distinctive features in the reflectance spectra (e.g., presence or absence of reddening phenomena) and (ii) the comprehension of the cosmic evolution of dust particles with particular emphasis on the role of water.

METHODOLOGY

The olivine crystals of this study (average size 5×4×3 mm^3 up to 1 cm for the longest direction) were sampled along the Mosteiros beach (São Miguel island, Azores) from basaltic and pyroclastic deposits of the Sete Cidades volcano. The Sete Cidades volcano lithologies spread from basaltic to trachytic passing from the pre-caldera to the caldera-forming phase and the post caldera (see ref [42]). The mafic rocks are classified as alkali-basalts and mainly contain phenocrysts of olivine, clinopyroxene and plagioclase in a fine-grained matrix. Olivine phenocrysts of mm size show euhedral shapes, a pale green color and their transparency is often reduced by the presence of inclusion phases such as spinel, plagioclase and ilmenite [42].

A set of three Mosteiros olivine crystals has been selected for chemical analyses by Scanning Electron Microscopy (SEM) Energy Dispersive X-ray Spectroscopy (EDS) to evaluate the homogeneity of the bulk chemistry and the mineral chemistry of the inclusion phases. Whereas another olivine crystal has been analyzed using Synchrotron Mössbauer spectroscopy to explore the possible occurrence of Fe^{3+} in the target material. Pulsed laser ablation was performed on one single crystal of olivine and high-resolution transmission electron microscopy followed by optical absorption spectroscopy, dynamic light scattering and ζ-potential analyses were performed on the resulting ablated material (see supporting info for more details about the dynamic light scattering and ζ-potential measurements). XPS measurements were carried out in parallel on another olivine crystal in order to evaluate the chemical composition variations before and after the ablation process.

Scanning Electron Microscopy

The three selected crystals were embedded in epoxy and carbon coated for the SEM- EDS analyses. The concentrations of major elements and, in some cases, NiO were measured by means of a Zeiss Gemini 500 instrument operating at 20 keV and equipped with a Bruker QUANTAX energy dispersive/wavelength dispersive detector.

Synchrotron Mössbauer Spectroscopy

Synchrotron Mössbauer spectroscopy was performed at the Nuclear Resonance Beamline ID18 [43], European Synchrotron Radiation Facility (Grenoble, France) using the setup reported by Potapkin et al. [44]. Room temperature Mössbauer spectra at the core and at the rim were collected on one Mosteiros olivine (0.5 × 0.5 × 0.3 mm^3). The experiments were carried out at ambient conditions with Be lenses and at velocities of ± 5 mm s^{-1} calibrated using a 25 μm thick natural α-iron foil. The X-ray beam-size was 9 × 4 μm^2. The linewidth was controlled before and after each sample measurement using $K_2Mg^{57}Fe(CN)_6$, whose Mössbauer spectrum consists of a single line. The data were then fitted with the software MossA using the full transmission integral and a Lorentzian-squared source line shape [45].

Liquid phase nanosecond pulsed laser ablation

One olivine single crystal was selected for the LP-PLA experiment and it was placed at the bottom of a polystyrene box filled with 4 ml of deionized water (type 1) to immerge it completely, with the liquid level at ca. 3 mm above it. LP-PLA experiments were performed with a Nd:YAG

laser at 1064 nm focused via a singlet lens onto the surface of the target and operating at 5 ns and 10 mJ per pulse with a repetition rate of 10 Hz. The ablation experiment was performed by manually moving the sample to perform a laser raster scan of the sample surface. In this procedure multiple laser ablations on the same spot might occur. The ablation duration was of about 10 hours.

X-ray photoelectron spectroscopy

XPS analyses were carried out at the Physics Department of the Politecnico di Milano on an olivine single crystal before and after the ablation. XPS measurements were performed in an ultrahigh-vacuum system (the base pressure was in the low 10^{-10} Torr range) equipped with a 150 mm hemispherical analyzer from SPECS GmbH operating at a pass energy of 20 eV [46]. Photoelectrons were excited by Al-Kα radiation (1486.6 eV), yielding an overall full width at half-maximum resolution of about 1 eV. The emitted electrons were collected at normal emission with the sample kept at room temperature. Wide energy scans and detailed scans on selected core level lines expected for the most abundant chemical species in the olivine structure (i.e., Si, Mg and Fe) were acquired.

Optical absorption spectroscopy

Absorption measurements on the colloidal solution have been carried out in the range 200-1100 nm (6.20 eV - 1.13 eV) and compared against reference colloidal solutions dispersed in deionized water (i.e. mesoporous silica [SiO_2] nanoparticles, brucite [$Mg(OH)_2$] nanoparticles, aluminum hydroxide [$Al(OH)_3$] nanoparticles, chrysotile [$Mg_3Si_2O_5(OH)_4$] nanotubes, and synthetic forsterite [Mg_2SiO_4] nanoparticles). Moreover, additional absorption analyses have been carried out as a function of the addition of known aliquots of sulfuric acid to study the suspensions behavior as a function of pH.

Electrodeposition and transmission electron microscopy

High-resolution transmission electron microscopy (HR-TEM) and EDS analyses were performed on the ablated nanoparticles deposited (i) directly from water suspension (2μl) and (ii) via electro deposition of the dried water suspension re-dispersed in ethanol (applied voltage: 20 V, electrode separation: 1 cm, duration: 20 minutes) onto C-coated Cu grids fixed by polypropylene clamps on 1×1 cm^2 indium-tin-oxide (ITO)-coated glass plates. TEM analyses have been performed with a JEOL JEM 2100Plus instrument at the Microscopy Platform of the University

of Milano-Bicocca. The instrument is equipped with a 9 MP Gatan Rio CMOS camera for image acquisition and an Oxford EDS system for chemical analysis. The instrument was operating at 200 kV with a LaB_6 source. Image processing was carried out using the GATAN Digital Micrograph software. In particular, direct measurement of the reflections from the selected area electron diffraction (SAED) patterns, processing of the SAED patterns using the DiffTools [47] and the direct measurement from the high-resolution bright field images coupled with the Fast Fourier Transform (FFT) have been performed in order to determine the interlayer spacings of crystalline nanoparticles and fragments.

RESULTS

Scanning electron microscopy analyses and Synchrotron Mössbauer spectroscopy

The olivine crystals from the "Mosteiros suite" are forsterite-rich [~Fo_{87}; ($Mg_{1.74}$, $Fe_{0.26}$) SiO_4] and contain plagioclase ($NaAlSi_3O_8$-$CaAl_2Si_2O_8$) and ilmenite ($FeTiO_3$) as inclusions phases. The FeO content for all the samples is constant and around 13 wt% (see Table S1), while Fe^{3+} was not detected by Synchrotron Mössbauer spectroscopy (Figure S1) and Ni concentration

is around 1300 ppm. These results are in agreement with chemical data reported by Beier et al. [42] on Azores olivines from the pre-caldera stage.

X-ray photoelectron spectroscopy

Wide XPS spectra of olivine before and after the ablation process are reported in Figure 1 with the main photoemission features from Fe, Si, Mg and O highlighted. Detailed scans of the Fe 2*p*, Si 2*p* and Mg 2*s* energy regions before and after the ablation process are reported in Figure 2. The binding energy scale is corrected by setting the binding energy (E_B) position of the C 1*s* peak from adventitious carbon to E_B= 284.8 eV as in Dukes et al. [20]. In Figure 2, the photoemission spectra are normalized to the intensity of the Si 2*p* lineshape.

After the ablation process, a drop in the Mg intensity is clearly visible in Figure 1 (consider, for instance, the signal from the Mg 1*s* and Mg Auger lines). Consistently, the relative intensity of the Mg 2*s* signal decreases in Figure 2b concomitant to an increase of the relative intensity of the Fe signal (Figure 2a). The binding energy positions of the photoemission features of Figure 2 are in agreement with the literature[20] and we can exclude the presence of metallic Mg, Si and Fe on the sample surface since that XPS spectra show no signals related to these phases. The Fe 2*p*

lineshape (Figure 2a) changes upon ablation, with a shift of the main photoemission peaks towards higher binding energy and the disappearance of the charge transfer screening structure (characterized by a satellite peak at about 715.5 eV [48-50] related to the presence of Fe^{2+} ions in the olivine matrix). This observation, together with the absence of any characteristic satellite structure, points towards a partial oxidation of Fe^{2+} into Fe^{3+} upon ablation, consistent with the formation of magnetite on the sample surface[50,51].

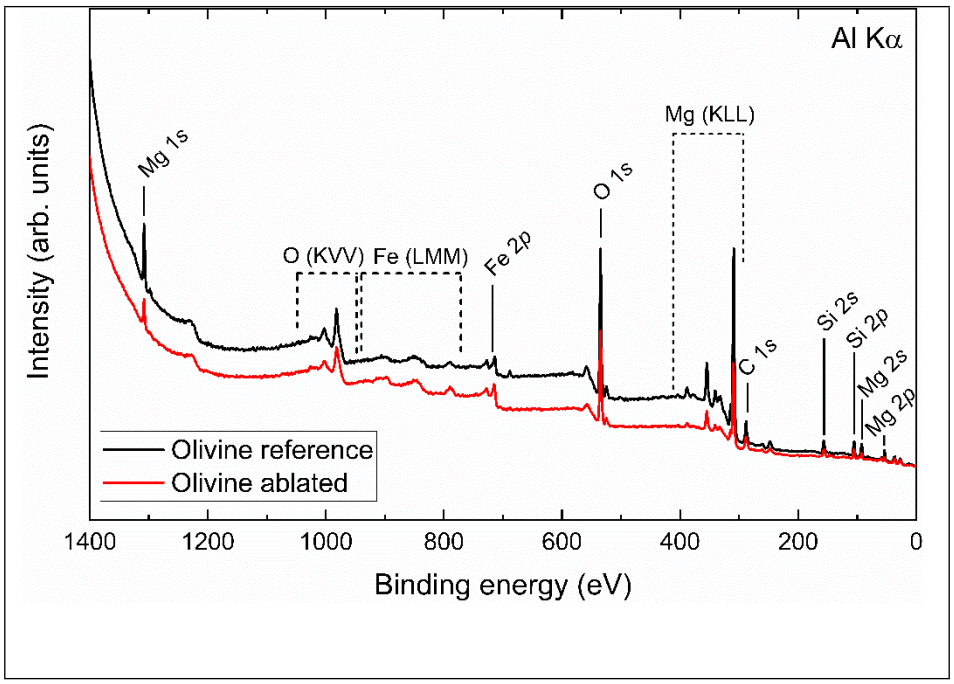

Figure 1. XPS wide energy scans acquired before (black) and after (red) the ablation process of the olivine single crystal. Dashed lines highlight the features related to Auger electron emission.

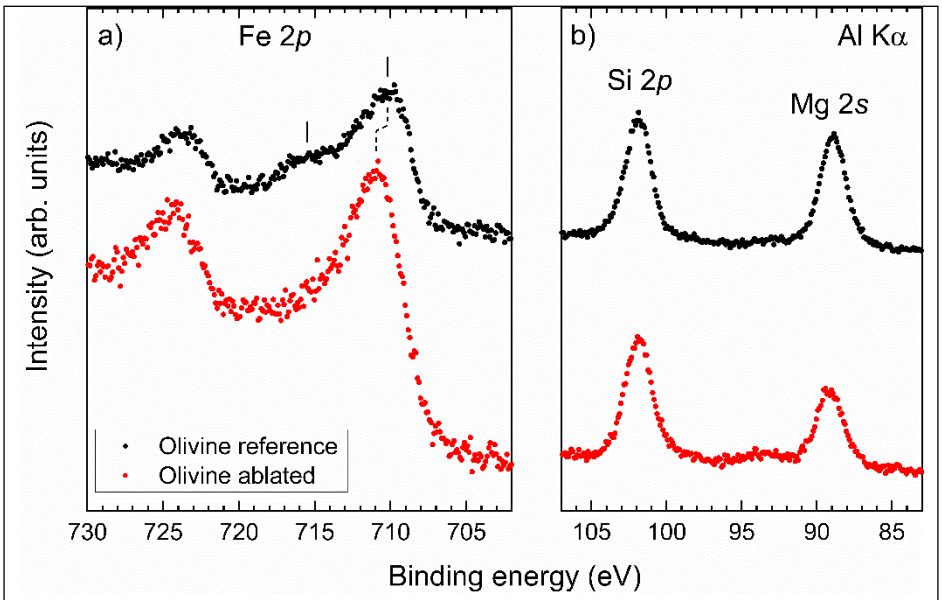

Figure 2. XPS spectra acquired on the a) Fe 2*p* and b) Si 2*p* and Mg 2*s* energy regions before (black) and after (red) the ablation process. Spectra have been normalized to the Si 2*p* photoemission intensity. Vertical lines in panel a) mark the energy position of the Fe 2*p*3/2 photoemission peak and its satellite.

Optical absorption spectroscopy

Optical absorption measurements on the resulting colloidal suspension composed by the material ejected from the olivine surface into the water show a main band around 218 nm. This feature is very similar to the "B_2 band" reported in several studies on silica glass [52,53] and ascribed to oxygen vacancies. This band is also a common feature in colloidal suspensions of synthetic forsterite, Mg/Al-hydroxides and chrysotile. Notably, the band peak is subjected to a slight shift due to the presence of different cationic species in addition or in substitution to silicon. In particular, the main absorption signal shows a gradual shift from 217 nm (silica mesostructured nanoparticles suspension signal) to about 218-219 nm when colloidal suspensions of synthetic forsterite, ablated olivine nanoparticles and chrysotile are measured. While the shift is larger when Mg- (222 nm) and Al- hydroxides (224 nm) are analysed (see Figure S2). Therefore, this behavior suggests a dependance of the signal on both the coordination and valence of the cation species. Moreover, the colloidal solution of olivine ejecta shows an additional and characteristic absorption

band around 270 nm, which is sensitive to pH. Indeed, it shifts progressively to 300 nm as the pH is reduced by the addition of a diluted solution of sulfuric acid (Figure S3). This signal could be due to the presence of SiO_2 nanoparticles together with ferric and ferrous oxides. These latter are dissolved by sulfuric acid liberating ferric and ferrous ions which, at acidic pH, give rise to absorption bands centered at 300 nm (see ref [54] SiO_2 nanoparticles; see refs [55,56] for magnetite nanoparticles and [57]).

High-resolution transmission electron microscopy

After the LP-PLA and optical spectroscopy analyses, the colloidal suspension was (i) drop-casted (2μl) onto a C-coated Cu grids and (ii) subjected to a drying process and re-dispersion in ethanol for the application of a constant electric field to promote electro-deposition of suspended nanoparticles onto C-coated Cu grids serving as anode and cathode. These grids were then analyzed by means of HR-TEM/EDS.

Drop-cast grid

Detailed HR-TEM imaging analyses on the drop-cast of the ejecta revealed the structural complexity of the ablated material. The size distribution varies from large globular aggregates of

hundreds of nanometers in diameters (~600 nm) to small nanoparticles of 4-10 nm in diameter (Figure 3 a-f) as also confirmed by the DLS analyses (see Figure S4). Moreover, large crystalline fragments of hundreds of nanometers are also present (Figure3 g-i).

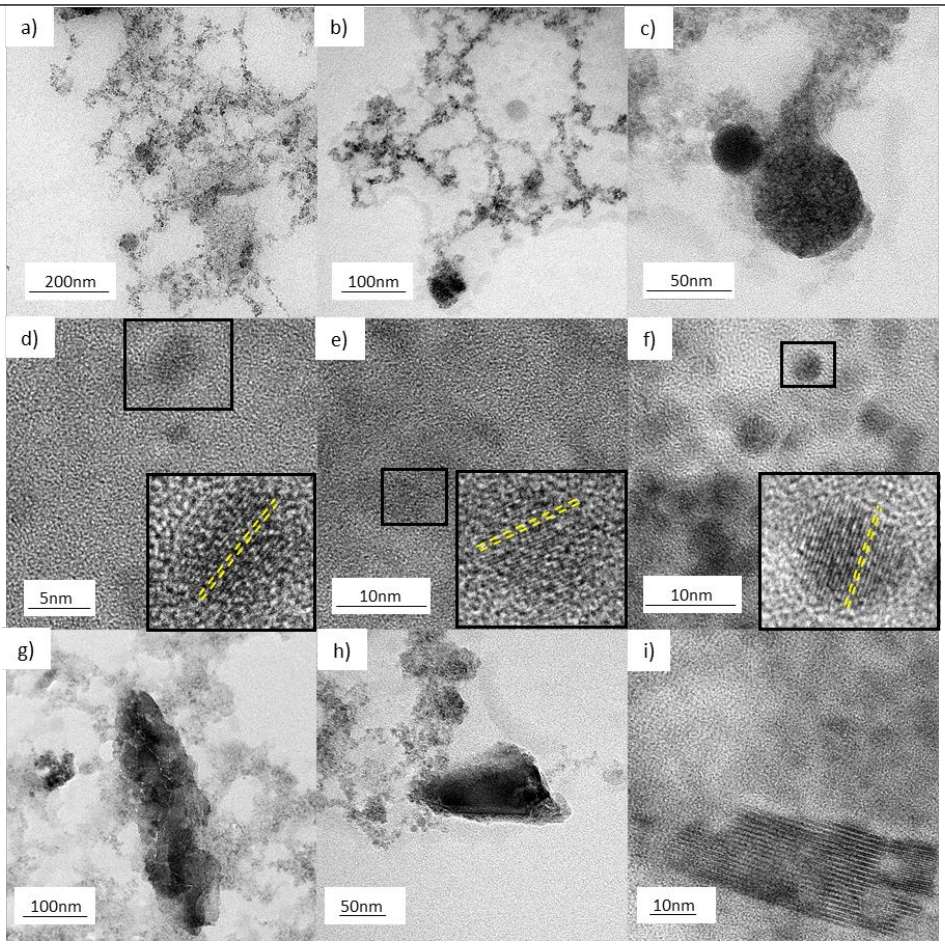

Figure 3. Bright field images of the drop-cast colloidal suspension: (a,b,c) Globular nanoparticle aggregates; (d,e,f) high-resolution images of the

aggregates in (a) showing the individual nanoparticles of about 4 to 10 nm in diameter and their lattice fringes as evident in the insets; (g,h,i) crystalline fragments.

High-resolution bright field images were collected in the region nearby the globular aggregates (as those reported in Figure 3 a-c) revealing the presence of spherical particles at the nanoscale (see Figure 3 d-f). The nanoparticles show evidence of lattice fringes pointing to their crystalline nature. Because of the low concentration of nanoparticles within the selected area aperture, their very small dimensions, and the high background due to the carbon membrane and amorphous material in general, diffraction rings were discontinuous and diffuse, and could not be profitably exploited. The interplanar distances of the crystalline nanoparticles were therefore obtained by the lattice fringe spacing in high-resolution images, which gave a systematic value around 2.1 ± 0.1 Å (value averaged on 12 measurements). Unfortunately, this datum alone was not sufficient to univocally identify the nanoparticles, since most candidate phases have at least one family of crystallographic planes with distances in this range. EDS spectra collected on the

nanoparticle aggregates show the presence of Fe, Mg, Si and O with sometimes a slight enrichment in Fe with respect to Mg, indicating a compositional change of the nano-ablated product with respect to the parent olivine (see Figure S5). On this basis, and considering the measured average d-spacing of 2.1 ± 0.1 Å, MgO (periclase, most intense reflection at 2.11 Å) and FeO (wustite, most intense reflection at 2.15 Å) are among the possible phases forming the ejecta material.

On the other hand, the average measurable interlayer spacings of the large fragment displayed in Figure 3i are 10.2(3) Å and 4.8(2) Å, which are consistent with (010) and (100) planes of olivine, respectively (Figure 4a). This same fragment also shows some clear effects of the ablation process such as local lack of periodicity and misorientation of the lattice planes (see Figure 4a). These features, along with the resulting EDS spectrum (Figure 4b), are consistent with fragments of ablated olivine.

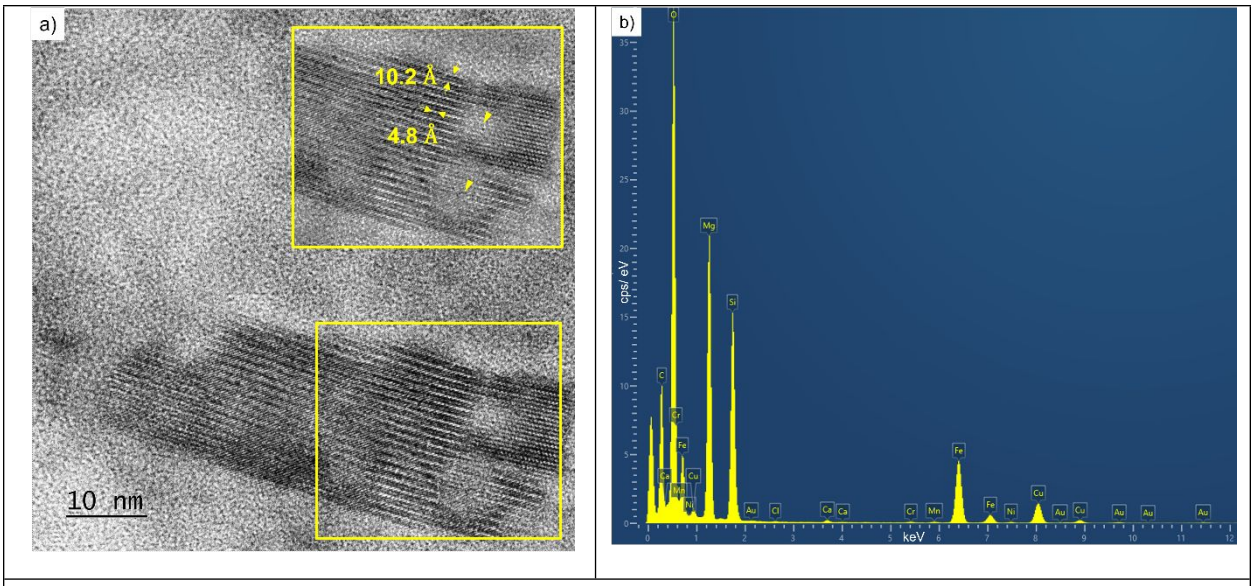

Figure 4. a) Large crystalline fragment found in the ablated product. It shows d-spacings of 10.2(3) and 4.8(2) Å consistent with the (010) and (100) planes of olivine, view along [001]. Effects of the ablation process are also evident as planes misorientation and lack of periodicity (yellow arrows in the top right inset). **b)** EDS spectrum.

Electro-deposition grids

Electro-deposition was performed in order to exploit the electrostatic properties of the suspended nanoparticles with the aim to promote their separation and, consequently, to allow for a better chemical characterization. The analysis of the ζ-potential of the ablated nanoparticles re-suspended in ethanol performed by dynamic light scattering methods showed a clear population

of charged particles centered at −30 mV (see Figure S6). Despite this evidence, after electro-deposition, nanoparticles were revealed in both the cathode and anode C- coated Cu grids (Figure 5). Moreover, the electro-deposition promoted the formation of a homogeneous layer of nanoparticles with sometimes sparse branched big aggregates (see Figure S7).

On the cathode, nanoparticles are found with an average diameter size of 4 ± 1 nm, while on the anode the size of the nanoparticle was 9 ± 3 nm (Figure 5a and c). The nanoparticles on both the electrodes give neater signals with respect to those of the drop-cast allowing for a diffraction analysis.

The SAED patterns acquired on the nanoparticle aggregates reported in Figure 5b and d show the coexistence of an amorphous fraction (diffuse haloes) together with a crystalline one (weak diffraction rings and spotted rings, see yellow arrows). Interlayer spacings of the crystalline nanoparticles have been determined from (i) HR lattice fringe images and (ii) SAED patterns. Among all the measured values four main d-spacings have been measured: 1.32 ± 0.01 Å (average of 2 measurements), 1.60 ± 0.01 Å (average over 3 measurements), 2.13 ± 0.06 Å (average of 44 measurements) and 2.52 ± 0.05 Å (average of 17 measurements). Moreover, in high-resolution bright-field images, each individual crystalline nanoparticle shows only one lattice fringe

corresponding to one of the four aforementioned d-spacings, while in the collected SAED patterns up to two simultaneous reflections among the four reported above can be observed (see yellow arrows in Figure 5b and d). The measured interlayer spacings are consistent with the most intense X-ray reflections of wustite, periclase, metallic Mg, magnetite, hematite, magnesioferrite and maghemite (see highlighted values in Table S2). The diffuse haloes are located close to the diffraction rings and have average d-spacings of 2.1 ± 0.1 Å, 1.2 ± 0.2 Å (Figure 5b) and 2.5 ± 0.1 Å, 1.56± 0.2 Å (Figure 5d), similar to those measured for the crystalline fraction [58,59].

Therefore, in order to narrow the range of the possible phases, we collected EDS spectra on both the electrodes in areas with a sufficient concentration of nanoparticles. The chemical analyses revealed the presence of only Mg, Si and O, whereas Fe was below the detection limit (see Figure S8). The higher amount of Mg with respect to Fe together with the measured d-spacings point out to a possible presence of periclase nanoparticles as dominant phase in the ejecta material.

Furthermore, it is worth noting that, despite showing the same morphology and chemical composition, the nanoparticles were found with smaller size on the cathode, while with larger size on the anode. This points to a dependence of the nanoparticle charge on its size due to their high surface-to-volume ratio [40,60,61].

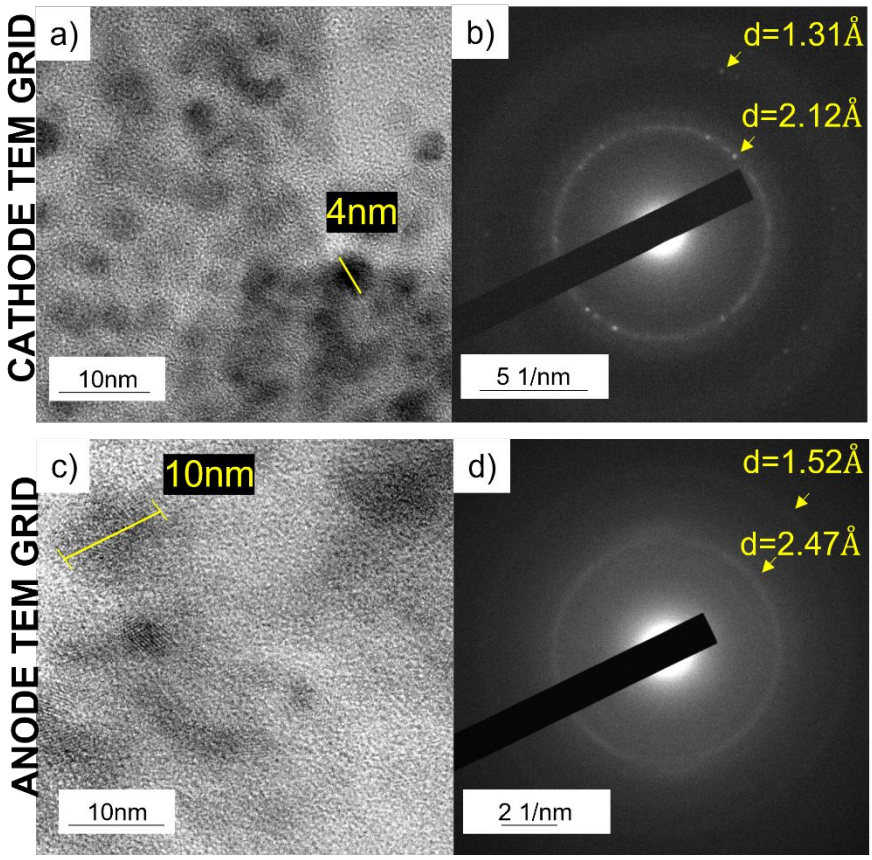

Figure 5. Bright field TEM and diffraction images of the cathode (a,b) and anode (c,d) grids. High-magnification images of the nanoparticles (a,c) and the corresponding diffraction signals (b,d).

DISCUSSION

Our multi methodological approach, combining the analysis of both the ablated material and the target, showed the occurrence of clear structural and chemical changes as a consequence of the simulation of space weathering in water environment. Specifically, the ablated material (ejecta) is made up by (i) a fraction of crystalline nanoparticles (4-10 nm in diameter) with diffraction signals mostly compatible with the presence of metallic Mg and/or periclase as the dominant phase with minor Fe-oxides; (ii) amorphous material (as evident from the diffuse halo in the diffraction images) with a composition close to the crystalline fraction and (iii) shocked crystalline olivine fragments of size of the order of 500-600 nm (see Figure 3 g-I and Figure 4).

On the other hand, the target is depleted in Mg and enriched in Fe, showing a partial oxidation of Fe^{2+} into Fe^{3+}, in agreement with the formation of magnetite domains on the sample surface.

The evidence of partial oxidation of Fe^{2+} into Fe^{3+} on the target surface is in net contrast with the results of similar ablation experiments on olivine samples performed in vacuum [17,18,22], where the authors report the occurrence of metallic Fe-nanoparticles. The presence of metallic iron particles together with the Mg removal from the target is explained by the thermal reduction mechanism in absence of a subsequent re-oxidation (see ref [22] for more details). Chemical

reduction is a common process also in water, promoted by hydrated electrons forming during plasma ignition which are potentially able to reduce both Fe and Mg into their metallic state [40]. These species might survive in water (or even only in air) as nanoparticles only if immediately capped by an inert layer. This layer has been demonstrated to be represented by silica in laser ablation experiments performed on Si targets immersed in metallic precursor solutions (Ag^+, Au^{3+}). These studies have shown that metastable species such as H_2SiO_2 can be formed as the result of the interaction of Si-rich targets and water, exhibiting the capability of reducing noble metal ions into metallic nanoparticles while oxidizing into silica forming a capping layer around them [57,62-66]. In our case, this process might be active in a region relatively far from the solid-liquid interface, while re-oxidation is promoted by the presence of radical species in the water environment in a region confined at the solid-liquid interface [67]. This might account for the fact that we have nanoparticles compatible with metallic Mg. However, by the analysis of the lattice spacing of the produced nanoparticles, we can confidently rule out the presence of metallic Fe. This observation can be explained by an apparent tendency of Fe-ions to remain bonded to the target, in contrast to the tendency of Mg-ions to detach from the target, as demonstrated by the

increase in the Fe-related signal and the simultaneous decrease in the Mg-related signal in XPS spectra (Figure 2).

Since the raster scanning of the target during the ablation process was performed by moving the stage manually, it is likely that the newly formed magnetite on the sample surface was also subjected to a subsequent ablation with its further transport into the colloidal suspension. Indeed, the measured spacings of the crystalline nanoparticles are also consistent with the presence of magnetite, in addition to the other abovementioned possible Mg and Fe phases (see TEM results session). However, the presence of Fe has been detected only in the drop-cast material, while it was below the detection limit on both cathode and anode grids (Figure S8). Therefore, the d-spacings measured on both cathode and anode TEM grids, even if compatible with the presence of magnetite and other Fe compounds (see Table S2), are likely due to Mg compounds (i.e., silica-capped metallic Mg and periclase). This evidence indicates that Fe-bearing nanoparticles do not acquire a substantial charge enabling their migration to the electrodes when re-dispersed in ethanol.

The presence of iron oxides (e.g., magnetite) and therefore the absence of metallic iron is consistent with an environment that experienced aqueous alteration during its history as occurred

for example on Mars or on carbonaceous chondrites parent body [68-71]. Moreover, in the outer space, a large number of bodies is (or has been) characterized by the presence of volatile-rich elements as well as hydrous minerals or water ices (e.g., Mars, Ceres, asteroids, comets) that affect the chemistry and physics of space weathering processes [15,29,72]. In particular, magnetite is quite ubiquitous on Earth and in planetary materials and it is often a marker for a variety of processes as for water-rock interactions (e.g., serpentinization, see ref [73] and references therein).

CONCLUSIONS

The coupling of the nanosecond liquid-phase pulsed laser ablation with the use of olivine single crystals as targets allows us to characterize both the shocked target and the ejecta material (i.e., colloidal suspension).

We provide a methodological approach to investigate space weathering processes in a water environment. We observe that the water environment triggers the partial oxidation of Fe^{2+} into Fe^{3+} in a region confined at the solid target-liquid interface, promoting the formation of

magnetite on the sample surface. On the other hand, Mg is easily removed, and the target results Mg-depleted (Fe-enriched) after the ablation process.

In the ablated material, we find crystalline fragments close to an olivine composition (i.e., starting material) together with amorphous and crystalline nanoparticles. The crystalline nanoparticles have diffraction signals compatible with the mainly occurrence of Mg- bearing phases (i.e., Mg metallic and periclase) with minor Fe- phases: from silica-capped metallic Mg to magnetite. The latter probably coming from the ablation of the newly oxidized iron at the solid-liquid interface. The diffuse diffraction signals present in the diffraction images (Figure 5) together with the EDS analyses are also consistent with the occurrence of the same phases, as reported above for the crystalline nanoparticles, but in an amorphous status.

The identification of magnetite on the olivine surface together with the occurrence of iron oxides and metallic Mg capped by a silica shell in the ablated material might represent evidence of a space weathering processes associated with an aqueous environment on planetary materials and asteroids. Moreover, it seems clear that iron has a weak tendency to escape the olivine surface and that the water environment triggers its oxidation. This is expected to affect reflectance spectra through the absence of features related to metallic iron nanoparticles and the lack of reddening

phenomena. Moreover, this has profound implications in several research fields from astrobiology to planetary geology.

Even if a lot of work is still required to better identify the ablated species in the ejecta material, we provide an unexplored procedure in the field of space weathering studies of astronomical silicates. This study also contributes to the development of the new research area focused on the study of space weathering and alteration processes in different environments with respect to those of the airless silicate bodies in the inner solar system.

ASSOCIATED CONTENT

Supporting Information

The Supporting Information is available free of charge at:

Chemical analyses (Table S1), Mössbauer spectra (Figure S1), Absorption spectra (Figure S2), Absorption spectra with addition of known aliquots of sulfuric acid (Figure S3), Dynamic light scattering measurements (Figure S4), TEM/EDS chemical analyses (Figure S5), Zeta potential measurement (Figure S6), Low magnification TEM images (Figure S7), d-spacing of reference chemical species (Table S2), EDS spectra (Figure S8) (PDF)

AUTHOR INFORMATION

Corresponding Authors

Mara Murri - *Department of Earth and Environmental Sciences, University of Milano-Bicocca, I-20126 Milano, Italy;*

Marcello Campione – Department of Earth and Environmental Sciences, University of Milano-Bicocca, I-20126 Milano, Italy;

Email: mara.murri@unimib.it; marcello.campione@unimib.it

Authors

Giancarlo Capitani - *Department of Earth and Environmental Sciences, University of Milano-Bicocca, I-20126 Milano, Italy*

Mauro Fasoli - *Department of Materials Science, University of Milano - Bicocca, I-20125 Milano, Italy*

Angelo Monguzzi - *Department of Materials Science, University of Milano - Bicocca, I-20125 Milano, Italy*

Alberto Calloni - *Department of Physics, Politecnico di Milano, I-20133 Milano, Italy*

Gianlorenzo Bussetti - *Department of Physics, Politecnico di Milano, I-20133 Milano, Italy*

Nadia Malaspina - *Department of Earth and Environmental Sciences, University of Milano-Bicocca, I-20126 Milano, Italy*

Notes

The authors declare no competing financial interest.

ACKNOWLEDGEMENTS

Alberto Paleari and Roberto Lorenzi are kindly acknowledged for their support in the setup of Nd-YAG laser. Tiziano Catelani is kindly acknowledged for his skillful operation of the SEM at the Department of Earth and Environmental Sciences of Milano-Bicocca. The Mössbauer

experiments were performed on beamline ID18 at the European Synchrotron Radiation Facility (ESRF), Grenoble, France. M.M, M.C and N.M are grateful to the Local Contact Dimitrios Bessas at the ESRF for providing assistance in using beamline ID18. MC acknowledges the contribution of FAQC grant n. 2018-ATESP-0010 by the University of Milano – Bicocca.

REFERENCES

(1) Saunders, R.W.; Plane, J. M. A photo-chemical method for the production of olivine nanoparticles as cosmic dust analogues. *Icarus* **2011**, *212*, 373-382, DOI:10.1016/j.icarus.2010.12.019.

(2) Ysard, N.; Jones, A. P.; Demyk, K.; Boutéraon, T.; Koehler, M. The optical properties of dust: the effects of composition, size, and structure. *Astronomy & Astrophysics* **2018**, *617*, DOI:10.1051/0004-6361/201833386.

(3) Hochella, M.F.; Lower, S. K.; Maurice, P. A.; Penn, R. L.; Sahai, N.; Sparks, D. L.; Twining, B. S. Nanominerals, mineral nanoparticles, and earth systems. *Science* **2008**, *319*, 1631-1635, DOI:10.1126/science.1141134.

(4) Signorile, M.; Zamirri, L.; Tsuchiyama, A.; Ugliengo, P.; Bonino, F.;Martra, G. On the Surface Acid–Base Properties of Amorphous and Crystalline Mg_2SiO_4 as Probed by Adsorbed CO, CO_2, and CD3CN. *ACS Earth Space Chem.* **2020**, *4*, 345-354, DOI:10.1021/acsearthspacechem.9b00271.

(5) Witt, A.N. Small and very small interstellar grains. *J. Geophys. Res. Space Phys.* **2000**, *105*, 10299-10302, DOI:10.1029/1999JA900208.

(6) Li, A. Cosmic crystals caught in the act. *Nature* **2009**, *459*, 173-175, DOI:10.1038/459173a.

(7) Escatllar, A.M.; Lazaukas, T.; Woodley, S. M.; Bromley, S. T. Structure and properties of nanosilicates with olivine (Mg_2SiO_4) N and pyroxene ($MgSiO_3$) N compositions. *ACS Earth Space Chem.* **2019**, *3*, 2390-2403, DOI:10.1021/acsearthspacechem.9b00139.

(8) Kamijo, F. A theoretical study on the long period variable star, III. formation of solid or liquid particles in the circumstellar envelope. *Publications of the Astronomical Society of Japan 15* **1963.**

(9) Li, A.; Draine, B. T. On ultrasmall silicate grains in the diffuse interstellar medium. *ApJ Letters* **2001**, *550*, DOI:10.1086/319640.

(10) Carrez, P.; Demyk, K.; Cordier, P.; Gengembre, L.; Grimblot, J.; D'Hendecourt, L.; Jones, A.P;Leroux, H. Low-energy helium ion irradiation-induced amorphization and chemical changes in olivine: Insights for silicate dust evolution in the interstellar medium. *Meteorit. Planet. Sci.* **2002**, *37*, 1599-1614, DOI:10.1111/j.1945-5100.2002.tb00814.x.

(11) Zamirri, L.; Macia Escatllar, A.; Mariñoso Guiu, J.; Ugliengo, P.; Bromley, S. T. What Can Infrared Spectra Tell Us about the Crystallinity of Nanosized Interstellar Silicate Dust Grains? *ACS Earth and Space Chem.* **2019**, *3*, 2323-2338, DOI:10.1021/acsearthspacechem.9b00157

(12) Henning, T. Cosmic silicates. *Annu. Rev. Astron. Astrophys.* **2010**, *48*, 21-46, DOI:10.1146/annurev-astro-081309-130815.

(13) Draine, B.T.; Lee, H. M. Optical properties of interstellar graphite and silicate grains. *ApJ* **1984**, *285*, 89-108., DOI: 10.1086/162480.

(14) Fogerty, S.; Forrest, W.; Watson, D. M.; Sargent, B. A.; Koch, I. Silicate composition of the interstellar medium. *ApJ* **2016**, *830*, DOI:10.3847/0004-637X/830/2/71.

(15) Pieters, C.M.; Noble, S. K. Space weathering on airless bodies. *J. Geophys. Res. Planets* **2016**, *121*, 1865-1884, DOI:10.1002/2016JE005128.

(16) Sasaki, S.; Nakamura, K.; Hamabe, Y.; Kurahashi, E.; Hiroi, T. Production of iron nanoparticles by laser irradiation in a simulation of lunar-like space weathering. *Nature* **2001**, *410,* 555-557, DOI:10.1038/35069013.

(17) Loeffler, M.J.; Baragiola, R. A.; Murayama, M. Laboratory simulations of redeposition of impact ejecta on mineral surfaces. *Icarus* **2008**, *196*, 285-292, DOI:10.1016/j.icarus.2008.02.021.

(18) Loeffler, M.J.; Dukes, C. A.; Christoffersen, R.; Baragiola, R. A. Space weathering of silicates simulated by successive laser irradiation: In situ reflectance measurements of Fo90, Fo99+, and SiO_2. *Meteorit. Planet. Sci.* **2016**, *51*, 261-275, DOI:10.1111/maps.12581.

(19) Thompson, M.S.; Loeffler, M. J.; Morris, R. V.; Keller, L. P.; Christoffersen, R. Spectral and chemical effects of simulated space weathering of the Murchison CM2 carbonaceous chondrite. *Icarus* **2019**, *319*, 499-511, DOI:10.1016/j.icarus.2018.09.022.

(20) Dukes, C.A.; Baragiola, R. A.; McFadden, L. A. Surface modification of olivine by H+ and He+ bombardment. *J. Geophys. Res. Planets* **1999**, *104*, 1865-1872, DOI:10.1029/98JE02820.

(21) Zamirri, L.; Corno, M.; Rimola, A.; Ugliengo, P.Forsterite surfaces as models of interstellar core dust grains: computational study of carbon monoxide adsorption. *ACS Earth Space Chem.* **2017**, *1*, 384-398, DOI:10.1021/acsearthspacechem.7b00041.

(22) Fazio, A.; Harries, D.; Matthäus, G.; Mutschke, H.; Nolte, S.;Langenhorst, F. Femtosecond laser irradiation of olivine single crystals: Experimental simulation of space weathering. *Icarus* **2018**, *299*, 240-252, DOI:10.1016/j.icarus.2017.07.025.

(23) Guiu, J.M.; Escatllar, A. M.; Bromley, S. T. How Does Temperature Affect the Infrared Vibrational Spectra of Nanosized Silicate Dust? *ACS Earth Space Chem.* **2021**, *5*, 812-823, DOI:10.1021/acsearthspacechem.0c00341.

(24) Sasaki, S.; Kurahashi, E.; Yamanaka, C.; Nakamura, K. Laboratory simulation of space weathering: Changes of optical properties and TEM/ESR confirmation of nanophase metallic iron. *Adv. Space Res.* **2003**, *31*, 2537-2542, DOI:10.1016/S0273-1177(03)00575-1.

(25) Fazio, A.; Matthäus, G.; Harries, D.; Mutschke, H.; Nolte, S.; Langenhorst, F. Reproducing space weathering of olivine by using high-energy femtosecond laser pulses. *In Frontiers in Ultrafast Optics: Biomedical, Scientific, and Industrial Applications XVII. International Society for Optics and Photonics.* **2017**, *10094*, DOI:10.1117/12.2252130.

(26) Schmidt, D.; Pollok, K.; Matthäus, G.; Nolte, S.; Langenhorst, F. Nanodeformation in enstatite single crystals: Simulation of micrometeoroid impacts by femtosecond pulsed laser experiments. . *Geochemistry* **2019**, *79*, DOI:10.1016/j.chemer.2019.125542.

(27) Campins, H.; Hargrove, K.; Pinilla-Alonso, N.; Howell, E.S.; Kelley, M.S.; Licandro, J.; Mothé-Diniz, T.; Fernández, Y.; Ziffer, J. Water ice and organics on the surface of the asteroid 24 Themis. *Nature* **2010**, *464*, 1320-1321, DOI:10.1038/nature09029.

(28) Rivkin, A.S.; Emery, J. P. Detection of ice and organics on an asteroidal surface. *Nature* **2010**, *464*, 1322-1323, DOI:10.1038/nature09028.

(29) Blewett, D.T.; Denevi, B.W.; Le Corre, L.; Reddy, V.; Schröder, S.E.; Pieters, C.M.; Tosi, F.; Zambon, F.; De Sanctis, M.C.; Ammannito, E.;Roatsch, T. Optical space weathering on Vesta: Radiative-transfer models and Dawn observations. *Icarus* **2016**, *265*, 161-174, DOI:10.1016/j.icarus.2015.10.012.

(30) Bu, C.; Lopez, G. R.; Dukes, C. A.; McFadden, L. A.; Li, J. Y.; Ruesch, O. Stability of hydrated carbonates on Ceres. *Icarus* **2019**, *320*, 136-149, DOI:10.1016/j.icarus.2017.12.036.

(31) Brownlee, D. et al. Comet 81P/Wild 2 Under a Microscope. *Science* **2006**, *314*, DOI: 10.1126/science.1135840.

(32) Fulle, M.B., J. Fractal dust constrains the collisional history of comets. *Monthly Notices of the Royal Astronomical Society,* 2017, *469*, DOI: 10.1093/mnras/stx971.

(33) Potapov, A.; Mutschke, H.; Seeber, P.; Henning, T.; Jäger, C. Low-temperature Optical Properties of Interstellar and Circumstellar Icy Silicate Grain Analogs in the Mid-infrared Spectral Region. *ApJ* 2018, *861*, DOI:10.3847/1538-4357/aac6d3.

(34) Potapov, A.; Jäger, C.; Henning, T. Temperature programmed desorption of water ice from the surface of amorphous carbon and silicate grains as related to planet-forming disks. *ApJ* 2018, *865*, DOI:10.3847/1538-4357/aad803.

(35) Draine, B.T. Interstellar Dust Grains. *Annu. Rev. Astron. Astrophys.* 2003, *41*, 241-289, DOI:10.1146/annurev.astro.41.011802.094840.

(36) Patil, P.P.; Phase, D.M.; Kulkarni, S.A.; Ghaisas, S.V.; Kulkarni, S.K.; Kanetkar, S.M.; Ogale, S.B.;Bhide, V.G. Pulsed-laser–induced reactive quenching at liquid-solid interface: Aqueous oxidation of iron. *Phys. Rev. Lett.* 1987, *58*, DOI:10.1103/PhysRevLett.58.238.

(37) Kanitz, A.; Kalus, M.R.; Gurevich, E.L.; Ostendorf, A.; Barcikowski, S.; Amans, D. Review on experimental and theoretical investigations of the early stage, femtoseconds to microseconds processes during laser ablation in liquid-phase for the synthesis of colloidal nanoparticles. *Plasma Sources Sci. Technol.* **2019**, *28*, DOI:10.1088/1361-6595/ab3dbe.

(38) Shih, C.Y.; Shugaev, M.V.; Wu, C.; Zhigilei, L.V. The effect of pulse duration on nanoparticle generation in pulsed laser ablation in liquids: insights from large-scale atomistic simulations. *Phys. Chem. Chem. Phys.* **2020**, *22*, 7077-7099, DOI:10.1039/d0cp00608d.

(39) Tabata, H.; Fujii, M.; Hayashi, S.; Doi, T.; Wakabayashi, T. Raman and surface-enhanced Raman scattering of a series of size-separated polyynes. *Carbon* **2006**, *44*, 3168-3176, DOI:10.1016/j.carbon.2006.07.004.

(40) Chen, Q.; Li, J.; Li, Y. A review of plasma–liquid interactions for nanomaterial synthesis. *J. Phys. D Appl. Phys.* **2015**, *48*, DOI:10.1088/0022-3727/48/42/424005.

(41) Svetlichnyi, V.A.; Shabalina, A.V.; Lapin, I.N.; Goncharova, D.A.; Kharlamova, T.S.; Stadnichenko, A.I. Comparative study of magnetite nanoparticles obtained by pulsed laser ablation in water and air. *Appl. Surf. Sci.* **2019**, *467-468*, 402-410, DOI:10.1016/j.apsusc.2018.10.189.

(42) Beier, C.; Haase, K.M.; Hansteen, T.H. Magma Evolution of the Sete Cidades Volcano, São Miguel, Azores. *J. Petrol.* 2006, *47*, 1375-1411, DOI:10.1093/petrology/egl014.

(43) Rüffer, R.; Chumakov, A. I. Nuclear resonance beamline at ESRF. *Hyperfine Interact.* 1996, *97*, 589-604, DOI:10.1007/BF02150199.

(44) Potapkin, V.; Chumakov, A. I.; Smirnov, G. V.; Celse, J. P.; Rüffer, R.; McCammon, C.; Dubrovinsky, L. The 57Fe synchrotron Mössbauer source at the ESRF. *Journal of synchrotron radiation* 2012, *19*, 559-569., DOI:10.1107/S0909049512015579.

(45) Prescher, C.; McCammon, C.; Dubrovinsky, L. MossA: a program for analyzing energy-domain Mössbauer spectra from conventional and synchrotron sources. *J. Appl. Crystallogr.* 2012 *45*, 329-331, DOI:10.1107/S0021889812004979.

(46) Berti, G.; Calloni, A.; Brambilla, A.; Bussetti, G.; Duo, L.; Ciccacci, F. Direct observation of spin-resolved full and empty electron states in ferromagnetic surfaces. *Rev. Sci. Instrum.* 2014, *85*, DOI:10.1063/1.4885447.

(47) Mitchell, D.R.G. DiffTools: Electron Diffraction Software Tools for DigitalMicrograph™. *Microsc. Res. Tech.* 2008 *71*,588-593, DOI: 10.1002/jemt.20591.

(48) Calloni, A.; Berti, G.; Brambilla, A.; Riva, M.; Picone, A.; Bussetti, G.; Finazzi, M.; Ciccacci, F.; Duo, L. Electron spectroscopy investigation of the oxidation of ultra-thin films of Ni and Cr on Fe(0 0 1). *J Phys Condens Matter* 2014, *26*, 445001, DOI:10.1088/0953-8984/26/44/445001.

(49) Brambilla, A.; Calloni, A.; Berti, G.; Bussetti, G.; Duò, L.; Ciccacci, F. Growth and Interface Reactivity of Titanium Oxide Thin Films on Fe(001). *J. Phys. Chem. C.* 2013, *117*, 9229-9236, DOI:10.1021/jp400159j.

(50) Gota, S.; Guiot, E.; Henriot, M.; Gautier-Soyer, M. Atomic-oxygen-assisted MBE growth of α− Fe_2O_3 on α− Al_2O_3 (0001): Metastable FeO (111)-like phase at subnanometer thicknesses. *Phys. Rev. B* 1999, *60*, DOI:10.1103/PhysRevB.60.14387.

(51) Seyama, H.;Soma, M. Fe 2p spectra of silicate minerals. *J Electron Spectros. Relat. Phenomena* 1987, *42*, 97-101, DOI:10.1016/0368-2048(87)85010-7.

(52) Skuja, L.N.; Streletsky, A. N.; Pakovich, A. B. A new intrinsic defect in amorphous SiO2: twofold coordinated silicon. *Solid state commun.* **1984**, *50*, 1069-1072, DOI:10.1016/0038-1098(84)90290-4.

(53) Tohmon, R.; Mizuno, H.; Ohki, Y.; Sasagane, K.; Nagasawa, K.; Hama, Y. Correlation of the 5.0- and 7.6-eV absorption bands in SiO_2 with oxygen vacancy. *Phys. Rev. B Condens. Matter* **1989**, *39*, 1337-1345, DOI:10.1103/physrevb.39.1337.

(54) Rawat, R.; Tiwari, A.; Vendamani, V.S.; Pathak, A.P.; Rao, S.V.; Tripathi, A. Synthesis of Si/SiO_2 nanoparticles using nanosecond laser ablation of silicate-rich garnet in water. *Opt. Mater.* **2018**, *75*, 350-356, DOI:10.1016/j.optmat.2017.10.045.

(55) Wang, Y.; Xu, C.; Chang, Y.; Zhao, L.; Zhang, K.; Zhao, Y.; Gao, F.; Gao, X. Ultrasmall superparamagnetic iron oxide nanoparticle for T 2-weighted magnetic resonance imaging. *ACS Appl. Mater. Interfaces* **2017**, *9*, 28959-28966, DOI:10.1021/acsami.7b10030.

(56) Roychowdhury, A.; Pati, S. P.; Kumar, S.; Das, D. Effects of magnetite nanoparticles on optical properties of zinc sulfide in fluorescent-magnetic Fe_3O_4/ZnS nanocomposites. *Powder Technol.* **2014**, *254*, 583-590, DOI:10.1016/j.powtec.2014.01.076.

(57) Loures, C.C.A.; Alcântara, M.A.K.; Filho, H.J.I.; Teixeira, A.C.S.C.; Silva, F.T.; Paiva, T.C.B.; Samanamud, G.R.L. Advanced Oxidative Degradation Processes: Fundamentals and Applications. *International Review of Chemical Engineering (IRECHE)* **2013**, *5*, DOI:10.15866/ireche.v5i2.6909.

(58) Wang, L. M.; Ewing, R. C. Ion beam-induced amorphization of (Mg, Fe) 2SiO4 olivine series: An in situ transmission electron microscopy study. *MRS Online Proceedings Library (OPL)* **1991**, *235*. DOI:10.1557/PROC-235-333

(59) Wang, L. M.; Ewing, R. C. Ion-beam-induced amorphization of complex ceramic materials—minerals. *MRS Bulletin* **1992**, *17*, 38-44. DOI:10.1557/S0883769400041270

(60) Barisik, M.; Atalay, S.; Beskok, A.; Qian, S. Size dependent surface charge properties of silica nanoparticles. *J. Phys. Chem. C* **2014**, *118*, 1836-1842, DOI:10.1021/jp410536n.

(51) Shi, Y.R.; Ye, M. P.; Du, L. C.; Weng, Y. X. Experimental determination of particle size-dependent surface charge density for silica nanospheres. *J. Phys. Chem. C* **2018**, *122*, 23764-23771, DOI:10.1021/acs.jpcc.8b07566.

(62) McCarthy, M.C.; Gauss, J. Exotic SiO(2)H(2) Isomers: Theory and Experiment Working in Harmony. *J. Phys. Chem. Lett.* **2016**, *7*, 1895-1900, DOI:10.1021/acs.jpclett.6b00632.

(63) Ermakov, V.A.; Jimenez-Villar, E.; Silva Filho, J.M.; Yassitepe, E.; Mogili, N.V.; Iikawa, F.; de Sa, G.F.; Cesar, C.L.; Marques, F.C. Size Control of Silver-Core/Silica-Shell Nanoparticles Fabricated by Laser-Ablation-Assisted Chemical Reduction. *Langmuir* **2017**, *33*, 2257-2262, DOI:10.1021/acs.langmuir.6b04308.

(64) González-Castillo, J.R.; Rodríguez-González, E.; Jiménez-Villar, E.; Cesar, C.L.; Andrade-Arvizu, J.A. Assisted laser ablation: silver/gold nanostructures coated with silica. *Appl. Nanosci.* **2017**, *7*, 597-605, DOI:10.1007/s13204-017-0599-2.

(65) Hoang, H.T.; Sertsova, A.A.; Marakulin, S.I.; Subcheva, E.N.; Zaitseva, M.P.; Yurtov, E.V. Manufacture of Magnesium Oxide Nanoparticles Coated with Silica Shells. *Russ. J. Inorg. Chem.* **2018**, *63*, 1414-1418, DOI:10.1134/s0036023618110074.

(66) Livan, P.; Öztürk, T. Carbon encapsulation of elemental nanoparticles by spark discharge. *J. Mater. Sci.* **2018**, *53*, 14350-14360, DOI:10.1007/s10853-018-2647-z.

(67) Broadhead, E.J.; Tibbetts, K.M. Fabrication of Gold-Silicon Nanostructured Surfaces with Reactive Laser Ablation in Liquid. *Langmuir* **2020**, *36*, 10120-10129, DOI:10.1021/acs.langmuir.0c01581.

(68) Ehlmann, B.L.; Mustard, J.F.; Murchie, S.L. Geologic setting of serpentine deposits on Mars. *Geophys. Res. Lett.* **2010**, *37*, DOI:10.1029/2010gl042596.

(69) Lee, M.R.; Lindgren, P. Aqueous alteration of chondrules from the Murchison CM carbonaceous chondrite: Replacement, pore filling, and the genesis of polyhedral serpentine. *Meteorit. Planet. Sci.* **2016**, *51*, 1003-1021, DOI:10.1111/maps.12644.

(70) Veneranda, M.; Lopez-Reyes, G.; Pascual Sanchez, E.; Krzesinska, A.M.; Manrique-Martinez, J.A.; Sanz-Arranz, A.; Lantz, C.; Lalla, E.; Moral, A.; Medina, J.; et al. ExoMars Raman Laser Spectrometer: A Tool to Semiquantify the Serpentinization Degree of Olivine-Rich Rocks on Mars. *Astrobiology* **2021**, *21*, 307-322, DOI:10.1089/ast.2020.2265.

(71) Smith, R.J.; McLennan, S.M.; Achilles, C.N.; Dehouck, E.; Horgan, B.H.N.; Mangold, N.; Rampe, E.B.; Salvatore, M.; Siebach, K.L.; Sun, V. X-Ray Amorphous Components in

Sedimentary Rocks of Gale Crater, Mars: Evidence for Ancient Formation and Long-Lived Aqueous Activity. *J. Geophys. Res. Planets* **2021**, *126*, DOI:10.1029/2020je006782.

(72) Potapov, A.; Bouwman, J.; Jäger, C.; Henning, T. Dust/ice mixing in cold regions and solid-state water in the diffuse interstellar medium. *Nat. Astron.* **2021**, *5*, 78-85, DOI:10.1038/s41550-020-01214-x.

(73) Izawa, M.R.M.; Cloutis, E.A.; Rhind, T.; Mertzman, S.A.; Applin, D.M.; Stromberg, J.M.; Sherman, D.M. Spectral reflectance properties of magnetites: Implications for remote sensing. *Icarus* **2019**, *319*, 525-539, DOI:10.1016/j.icarus.2018.10.002.